

## Observation of high $T_c$ one dimensional superconductivity in 4 angstrom carbon nanotube arrays

Bing Zhang, Yang Liu, Qihong Chen, Zhiping Lai, and Ping Sheng

Citation: *AIP Advances* **7**, 025305 (2017); doi: 10.1063/1.4976847

View online: <http://dx.doi.org/10.1063/1.4976847>

View Table of Contents: <http://aip.scitation.org/toc/adv/7/2>

Published by the [American Institute of Physics](#)

---

---

# HAVE YOU HEARD?

Employers hiring scientists and  
engineers trust

**PHYSICS TODAY | JOBS**

[www.physicstoday.org/jobs](http://www.physicstoday.org/jobs)



## Observation of high $T_c$ one dimensional superconductivity in 4 angstrom carbon nanotube arrays

Bing Zhang,<sup>1</sup> Yang Liu,<sup>2</sup> Qihong Chen,<sup>1</sup> Zhiping Lai,<sup>2,a</sup> and Ping Sheng<sup>1,a</sup>

<sup>1</sup>Department of Physics, Hong Kong University of Science and Technology, Clear Water Bay, Kowloon, Hong Kong, China

<sup>2</sup>Division of Physical Sciences and Engineering, King Abdullah University of Science and Technology (KAUST), Thuwal 23955-6900, Saudi Arabia

(Received 7 November 2016; accepted 6 February 2017; published online 14 February 2017)

The only known approach to fabricate large, uniform arrays of 4-Å single wall carbon nanotubes (SWNTs) is by using zeolite crystals as the template, in which the nanotubes are formed by chemical vapor deposition inside the linear channels of the  $\text{AlPO}_4\text{-5}$  (AFI for short) zeolite. However, up to now the pore filling factor has been very low, as evidenced by the weight percentage of carbon in thermal gravimetric analysis (TGA) measurements. In this work, we show that by using a new, micro-platelet AFI crystals as the template, combined with the use of a new CVD process, we can increase the TGA result to 22.5wt%, which translates to a pore filling factor of 91%. We have observed one dimensional (1D) superconductivity in such samples. The temperature dependence of resistance shows a smooth decreasing trend below 60 K, and the differential resistance displays a gap that disappears above the 1D superconducting initiation temperature. The observed behaviour is shown to agree very well with the theoretical predictions of 1D superconductivity. © 2017 Author(s). All article content, except where otherwise noted, is licensed under a Creative Commons Attribution (CC BY) license (<http://creativecommons.org/licenses/by/4.0/>). [<http://dx.doi.org/10.1063/1.4976847>]

### I. INTRODUCTION

The discovery of carbon nanotubes<sup>1,2</sup> has propelled a tremendous amount of study on their electrical,<sup>3,4</sup> optical<sup>5,6</sup> and mechanical properties,<sup>7,8</sup> attendant with an increasingly diverse portfolio of applications.<sup>9–12</sup> With a very large length-to-diameter ratio, carbon nanotubes constitute an ideal one-dimensional material. Theoretical calculations<sup>13,14</sup> have predicted stability for carbon nanotube diameters as small as 4 Angstroms, and such small carbon nanotubes were indeed found experimentally.<sup>15,16</sup> Arrays of the 4 Å single wall carbon nanotubes (SWNTs) were synthesized inside the linear channels of zeolite crystals. They have been experimentally characterized by polarized and resonant Raman scattering,<sup>17</sup> optical absorption spectra,<sup>18</sup> as well as visualized by transmission electron microscope images.<sup>16</sup> By comparing the experimental observations with first principle calculations,<sup>19</sup> three types of 4 Å SWNTs were identified: (5,0), (3,3), (4,2). Such thin carbon nanotubes have displayed superconducting characteristics<sup>20,21</sup> that can result from the large curvature effect that opens channels for the electron–phonon coupling.<sup>22</sup> There have been many theoretical studies on carbon nanotube superconductivity.<sup>23–26</sup> For the superconductivity in 1D systems, it is well-known that owing to the thermally activated phase-slip mechanism<sup>27,28</sup> and macroscopic quantum tunneling (MQT),<sup>29–31</sup> the resistance would decrease smoothly as a function of temperature, and there is always finite resistance at finite temperatures.

The specific zeolite we used for the fabrication of 4 Å SWNT arrays was the  $\text{AlPO}_4\text{-5}$  (AFI). Its framework comprises alternating tetrahedral  $(\text{AlO}_4)^-$  and  $(\text{PO}_4)^+$  groups that form linear channels

<sup>a</sup>[zhiping.lai@kaust.edu.sa](mailto:zhiping.lai@kaust.edu.sa) (Zhiping Lai), [sheng@ust.hk](mailto:sheng@ust.hk) (Ping Sheng).

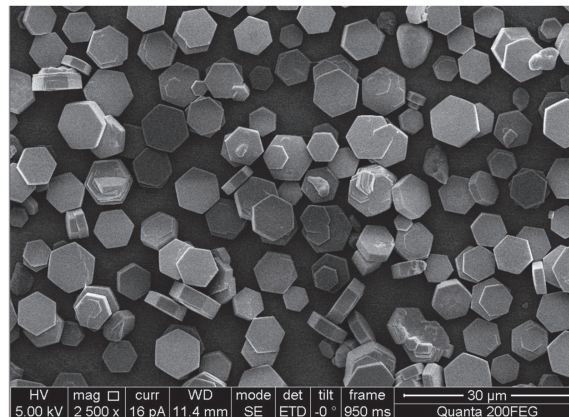


FIG. 1. A scanning electron micrograph (SEM) image of the micro platelet AFI crystals. They are  $\sim 5$  to 7 microns across and 2 microns thick.

along the  $c$ -axis with an inner diameter of 0.73 nm, and which exhibit a triangular lattice structure in the  $ab$  plane with a center-to-center separation between the nearest channels of 1.37 nm. AFI crystals are electrically insulating and optically transparent from the ultraviolet to near-infrared, and thermally stable up to 1200°C. Initially, 4 Å SWNTs were grown by pyrolysis of precursor materials trimethylamine (TPA). However, the weight percentage of carbon nanotubes (over the total mass of AFI frame containing carbon nanotubes) obtained by this approach was only 1.5wt%, which translated to a  $\sim 4.5\%$  filling factor of carbon nanotubes inside channels of AFI. Even with the poor sample quality, 1D fluctuating superconductivity of 4 Å SWNTs was discovered.<sup>20</sup> Subsequently, chemical vapour deposition (CVD) was used to improve the filling factor of 4 Å SWNTs inside the AFI. In this approach, the precursor TPA molecules were burned off in oxygen atmosphere. Subsequently a carbon source, such as ethylene, was introduced into the channels of AFI. The carbon source would decompose at high temperatures to form the 4 Å SWNTs. By this CVD approach the weight percentage of carbon as measured by thermal gravimetric analysis (TGA) can be raised to a maximum of 10.0wt%.<sup>32</sup> However, most of channels inside the AFI are empty, and carbon nanotubes would mostly be far-separated from each other.

In this work, we report that by using a new type of platelet-shaped crystals of AFI (as shown in Fig. 1) with a thickness of  $\sim 2$  microns and the  $c$ -axis of the channels perpendicular to the platelets' flat surface, the permeability of the template to the carbon source can be greatly improved. Hence by just repeating the past CVD procedure the TGA result can be readily raised to  $\sim 16\text{wt}\%$ . On that basis, we have further developed an approach in which the carbon sources ethylene ( $\text{C}_2\text{H}_4$ ) and methane ( $\text{CH}_4$ ) were used in successive CVD processes. By using this new approach on the platelet-shaped crystals, the carbon content can be improved to 22.5wt%, which translates to a pore filling factor of 91%. We have measured the optical and transport properties of 4 Å SWNTs. The radial breathing mode (RBM) signals in the Raman spectra are obvious, and the transport data showed 1D superconductivity behaviour initiating at around 60 K. Such a high initiation temperature is attributed to the high pore filling factor and the resulting effective dielectric screening of electron-electron interaction as shown theoretically.<sup>24</sup>

## II. EXPERIMENTAL

Previous AFI crystals used for the fabrication of 4-Angstrom carbon nanotubes were about 100 microns in diameter and 500 microns in length. More recently we have succeeded in synthesizing micro-platelet AFI crystals (see Appendixes for more details), which are only 2 microns thick and 5-6 microns in their lateral dimensions. These new AFI crystals have good quality as they contain fewer defects, and the short length of the straight pores, 2 microns, means that the permeability is greatly enhanced for the carbon source(s) in the CVD processes. These factors are crucial for achieving the high pore filling factor of 4 Å SWNTs. Three different CVD processes were used to fabricate the

carbon nanotubes inside the pores of the platelet AFI crystals: (a) using  $C_2H_4$  as the carbon source, (b) using  $CH_4$  as the carbon source, and (c) using both  $C_2H_4$  and  $CH_4$  as carbon sources in two successive rounds. Details of the CVD processes can be found in the Appendixes section. Method (c) has led to a high pore filling factor of 91%.

### III. RESULTS AND DISCUSSION

#### A. Raman spectra and TGA characterization of 4 Å SWNTs

We have measured the Raman spectra by the JobinYvon T64000 micro-Raman system with a laser wavelength of 514.5 nm. Since the 4 Angstrom SWNTs are marginally stable, hence if they are taken out from the AFI template (e.g., by dissolving the template), they would become unstable and turn into graphene nanoribbon. Therefore we measure the Raman spectra of Angstrom SWNTs embedded in AFI template. In fact the AFI template does not influence the Raman spectrum measurement of SWNTs as illustrated in Fig. 2 (the red line in 2(a)), since the signals of the empty AFI template are much weaker than the signals of SWNTs.

As shown in Figs. 2, 3, and 4, SWNTs fabricated by different carbon sources have similar features in the Raman spectra. However, it is worth noting that the measured Raman spectra are distinct from each other in small features. The peaks in the region of  $500\text{-}600\text{cm}^{-1}$  are the radial breathing modes (RBM).<sup>33</sup> The RBM originates from the coherent vibration of the carbon atoms along the radial direction that is unique to carbon nanotubes. Therefore RBM is an important signature of carbon nanotubes. Inside the channels of AFI, there are only three types of SWNTs: the zigzag (5, 0), the

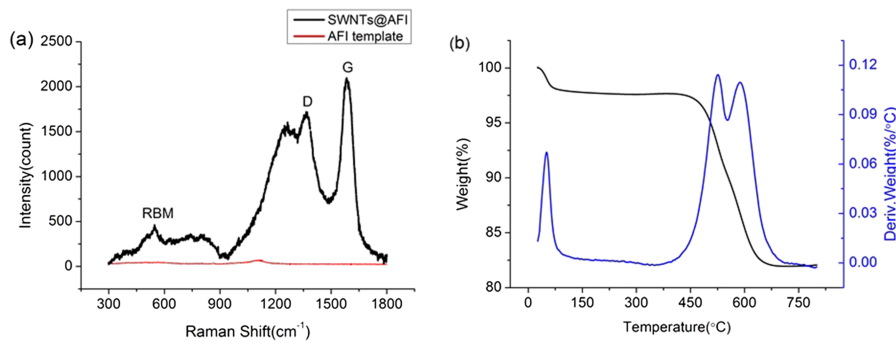


FIG. 2. Characteristics of 4 Å SWNTs fabricated with 6 atmospheres of ethylene as the carbon source. (a) Raman spectra of the sample with the labeled peaks. Here the red line is the Raman signal from the empty AFI zeolite template. It is seen that the template cannot affect the Raman signal of the carbon nanotubes, owing to its low level of the Raman signal. (b) TGA of SWNTs@AFI, which shows that the carbon content is 16.0wt%, corresponding to a filling factor of 60%. The blue curve in the right panel shows the derivative of the black curve.

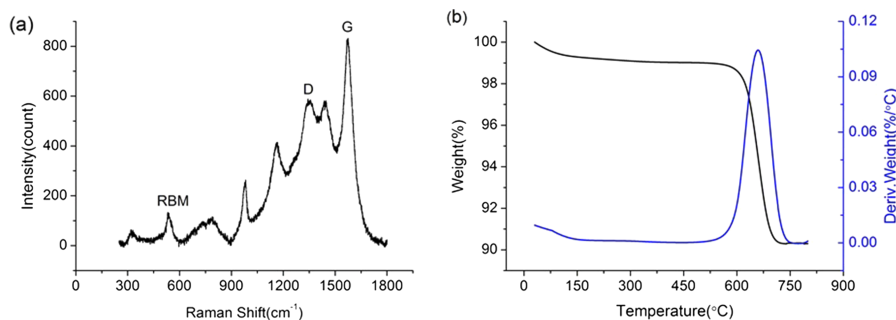


FIG. 3. Characteristics of 4 Å SWNTs fabricated with 6 atmospheres of methane as the carbon source. (a) Raman spectra. (b) TGA of SWNTs@AFI, which shows that the carbon content is 8.8wt%, corresponding to a filling factor of 30%. The blue curve in the right panel shows the derivative of the black curve.

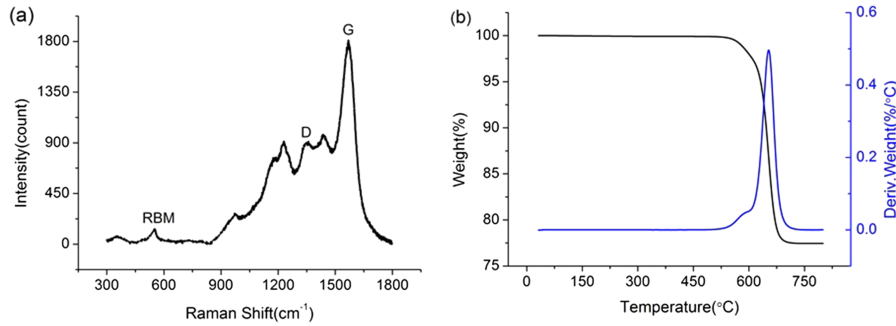


FIG. 4. Characteristics of 4 Å SWNTs fabricated with both ethylene and methane. (a) Raman spectra. (b) TGA of SWNTs@AFI, which shows that the carbon content is 22.5%, corresponding to filling factor of 91%. The blue curve in the right panel shows the derivative of the black curve. In this particular case, it is seen that the blue curve shows a sharp peak.

armchair (3, 3) and the chiral (4, 2).<sup>19</sup> They have diameters of 0.393 nm, 0.407 nm and 0.414 nm, respectively. Typical RBM range is 100–350  $\text{cm}^{-1}$ , but for 4 Angstrom SWNTs the RBM range is 500–600  $\text{cm}^{-1}$  due to the ultra-small diameter. We note that normally  $\omega_{RBM} = A/d + B$  is a useful empirical formula when  $d > 1$  nm. However, for SWNTs with 4 Angstrom diameter their RBM frequency is not simply inversely proportional to the CNT diameters. Here the chirality dependence of RBM for 4 Angstrom SWNTs were previously calculated by the CASTEP pseudopotential module in Material Studio as presented in Ref. 29. The RBM peak at 550  $\text{cm}^{-1}$  is attributed to the (3,3) carbon nanotubes, while the RBM peak at 534  $\text{cm}^{-1}$  is attributed to (5,0) carbon nanotubes. For SWNTs fabricated with  $\text{C}_2\text{H}_4$  as the carbon source the RBM peak at 550  $\text{cm}^{-1}$  is strong, while for SWNTs produced with  $\text{CH}_4$  the RBM peak at 534  $\text{cm}^{-1}$  is strong. For SWNTs fabricated with both  $\text{CH}_4$  and  $\text{C}_2\text{H}_4$  the strong RBM peak is also located around 550  $\text{cm}^{-1}$ .

The peaks in the range of 1100–1650  $\text{cm}^{-1}$  are the G band<sup>33</sup> and D band. G band contains two main components,<sup>34</sup>  $G^+$  and  $G^-$ , which arise from the vibrations of carbon atoms along the tube axis and the circumferential direction, respectively.  $G^+$  is located around 1600  $\text{cm}^{-1}$  while the  $G^-$  peaks (1160  $\text{cm}^{-1}$ , 1230  $\text{cm}^{-1}$ , 1441  $\text{cm}^{-1}$ ) are chirality and diameter dependent.<sup>31</sup> The peak around 1350  $\text{cm}^{-1}$  is the D band which arises from the defects in the structure of carbon nanotubes. A lower D band peak indicates a lower concentration of defects in the sample. We have tried to adjust the fabrication conditions to minimize the defects. The relatively large D band is the result of growing the nanotubes without the catalysts, and so far the large D band is common to all the template-growth efforts. In three types of fabrication methods, SWNTs fabricated with ethylene and methane in successive rounds have lower defect concentration than that of the other two methods. There is a peak around 986  $\text{cm}^{-1}$  which is called intermediate frequency mode. This mode is a combination mode of one optical and one acoustic phonon.<sup>35</sup> Such intermediate frequency mode is Raman-inactive for large carbon nanotubes, but can be active for small diameter carbon nanotubes.

TGA was used to assess the carbon content of SWNTs@AFI samples. In the measurements, samples of SWNTs@AFI were heated in the air from room temperature to 800°C with a heating rate of 2°C/min by Q5000 TGA. The sample weight was constantly monitored by a microbalance. By burning off the carbon inside the AFI crystals, we obtained the carbon content from the difference in weight before and after the heating process. After getting the carbon content we can translate it into the pore filling factor which is defined as the pores filled with SWNTs divided the total pores of AFI. The calculation of pore filling factor can be done in one unit cell of AFI crystals ( $\text{Al}_{12}\text{P}_{12}\text{O}_{48}$ ) by solving the following equation:

$$\text{carbon content} = \frac{W_{CNT}(f)}{W_{CNT}(f) + W_{AFI}}, \quad (1)$$

where  $f$  is the pore filling factor,  $W_{AFI}$  is weight of one unit cell of AFI, and  $W_{CNT}$  is the weight of carbon nanotubes within the same unit cell length. The latter is a function of pore filling factor  $f$ .

For the SWNTs@AFI sample grown with  $\text{C}_2\text{H}_4$  as the carbon source, the carbon content was 16.0wt%, which represents a significant improvement of ~6wt% from the previous maximum<sup>29</sup> and

corresponds to a pore filling factor of 60%. We note that there are two peaks in the derivative curve as shown in Fig. 2(b). The first peak is around 500°C. It can be attributed to small hydrocarbon molecules left over from the decomposition of ethylene. The second high peak around 600°C is attributed to the carbon nanotubes. This result tells us that there are not only SWNTs but also some small hydrocarbon molecules in the sample grown with C<sub>2</sub>H<sub>4</sub>. In contrast, for SWNTs@AFI sample heated with CH<sub>4</sub> as the carbon source the TGA result is just 8.8wt%, corresponding to a pore filling factor of 30% as shown in Fig. 3. However, in the derivative curve there is only one peak. Hence for SWNTs@AFI fabricated with CH<sub>4</sub> most of the carbon is in the form of SWNTs. For the sample fabricated by using ethylene and methane as the successive carbon sources, the carbon content can reach 22.5wt%, corresponding to a pore filling factor of 91% (see Fig. 4). In the derivative curve, the low temperature peak is seen to be negligible while the higher temperature peak is very sharp. This can mean that the majority of carbon in this sample is in the form of SWNTs. The disappearance of the low temperature calorimetry peak also offers a hint to the reason for the high TGA result. Basically, in the second heating with methane at 800° C, the small hydrocarbon molecules were converted to nanotubes. By driving off the hydrogen, more space was created in the channels for the growth of nanotubes.

## B. Observation of high $T_c$ 1D superconductivity

The electrical transport properties of our samples were studied by first fabricating the devices from the CVD-heated samples using the method (c), in which we have achieved 91% pore filling factor. Focused ion beam (FIB) was used to make the four-terminal configuration as shown in Fig. 5. Measurement of the fabricated device was carried out by using the Physical Property Measurement System (PPMS). A Keithley 6221 was used as the current source and a SR850 lock-in was used as voltmeter to measure the resistance and differential resistance of carbon nanotubes.

The sample resistance, measured in the four terminals configuration with a current of 50 nA, is plotted as a function of temperature in Figure 6. We can see that the resistance slightly increased from 108Ω to 132Ω when the sample was cooled down from room temperature to 85 K, which implies the existence of some weak links (arising from the discontinuities and defects in the carbon nanotubes) between 4 Å SWNTs. Then the resistance started to decrease smoothly but it did not go to zero when temperature was reduced to 2 K. The resistance did not change when a magnetic field up to 9 T was applied. All these features indicate one-dimensional superconductivity in 4 Å SWNT arrays with a small cross section, which can be described by Langer-Ambegaokar-McCumber-Halperin (LAMH)<sup>27,28</sup> theory and macroscopic quantum tunneling (MQT)<sup>29–31</sup> theory. There have been many experimental studies about the superconductivity in multi-walled nanotubes (MWNTs),<sup>36,37</sup> in double-walled nanotubes (DWNTs)<sup>38</sup> and in SWNTs.<sup>39</sup> For 1D superconducting systems with very small cross sections, thermally activated phase slips are known to induce energy barrier in the free energy of the systems. The energy barrier can be written as  $\Delta F = (8\sqrt{2}/3) (H_C^2/8\pi) \sigma \xi$  (see [supplementary material](#), Fig. S2, in which the barriers between the metastable states, characterized by the winding number  $n$ , are shown), where  $H_C$  and  $\xi$  are the thermodynamic critical field and the coherence length,  $\sigma$  is the cross sectional area of the superconductor. This means that the smaller the diameter of CNTs the smaller would be the energy barrier, thereby leading to enhanced phase

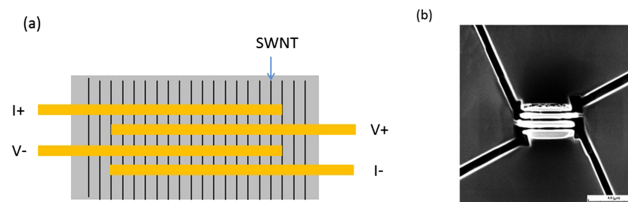


FIG. 5. Device for transport measurement. (a) Schematic illustration of the four-terminal geometry etched by the FIB on the sidewall of a platelet crystal standing on its side. (b) A four-terminal electrical measurement configuration image taken by the FIB. In such electrical measurements, constant current was supplied, with the voltage probes measuring the voltage drop across a very narrow gap, typically 100 nm in width.

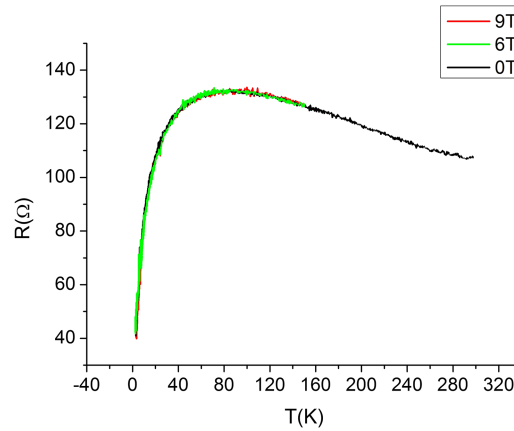


FIG. 6. Temperature dependence of resistance. The sample was measured by four terminals configuration with different applied magnetic field.

slip fluctuations. This phase slip mechanism leads to a resistance temperature dependence given by

$$R_{LAMH} = R_N \exp(-\Delta F/k_B T) = R_N \exp \left[ -A \frac{T_C}{T} \left( 1 + \frac{T}{T_C} \right)^2 \left( 1 - \frac{T}{T_C} \right)^{3/2} \right], \quad (2)$$

where  $A$  is a dimensionless constant. Hence the resistance of 1D superconductors is predicted to decrease smoothly as a function of temperature if the parameter  $A$  is relatively small. This is in contrast to 3D superconductors whose resistance can drop abruptly at the transition temperature. For the case of 4 Å SWNTs the diameter is ultra-small, which leads to very small energy barrier and large fluctuations. Therefore the resistance decreased quite smoothly and doesn't reach zero even at 2 K. In contrast, the 1D superconductivity of MWNTs (with an outer diameter of 7.4 nm fabricated inside nanoporous alumina) reported by I. Takesue *et al.*<sup>37</sup> exhibited a relatively sharp drop to zero resistance, which is owed to the fact that the cross sectional area of these MWNTs is many times larger than that of individual 4 Å SWNTs. Therefore these MWNTs have a much larger energy barrier and their resistance can more quickly decrease to zero.

As shown in Fig. 7, LAMH theory (Eq. (2)) is used to fit the data which agrees well with experiment results. The parameter values obtained are  $T_c = 60$  K,  $A = 0.09$ . The especially small magnitude of  $A$  can be due to the small cross sectional area of the nanotube bundle. However, we note that the LAMH fit deviates from the experimental data at low temperature regime (lower than 10 K). This indicates although thermally activated phase slips dominate near the superconducting transition temperature, macroscopic quantum tunneling (MQT) should be considered in the low temperature regime. Giordano<sup>29</sup> gave a heuristic argument which suggest that the resistance from MQT follows a form similar to (2), except that the energy scale  $k_B T$  is replaced by  $\hbar/\tau_{GL}$ . Therefore,

$$R_{MQT} = const \cdot R_N \exp(-a\Delta F\tau_{GL}/\hbar) \quad (3)$$

where  $\tau_{GL} = \pi\hbar/8k(T_C - T)$  is the characteristic relaxation time in the time-dependent Ginzburg-Landau theory, and  $a, const$  are numerical factors. As the resistance is proportional to the rate of phase slips, and the rates from the two mechanisms of phase slips are obviously additive, hence the total resistance of the 1D superconductor is given by  $R = R_{LAMH} + R_{MQT}$ . After simplification, we get

$$\frac{R}{R_N} = B \exp \left[ -A_1 \frac{T_C}{T} \left( 1 + \frac{T}{T_C} \right)^2 \left( 1 - \frac{T}{T_C} \right)^{\frac{3}{2}} \right] + (1 - B) \exp \left[ -A_2 \frac{T_C}{T_C - T} \left( 1 + \frac{T}{T_C} \right)^2 \left( 1 - \frac{T}{T_C} \right)^{\frac{3}{2}} \right], \quad (4)$$

where  $A_1, A_2, B$  are dimensionless parameters. This formula is used to fit the experimental data as shown in Fig. 7. The agreement between theory and experiment is excellent. The parameter values obtained by the fit are  $A_1 = 0.1, A_2 = 0.13$ , and  $B = 0.89$ .

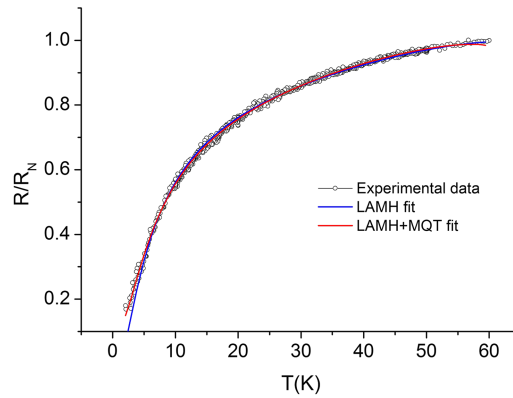


FIG. 7. The fitting of temperature dependence of resistance. The open circles represent experimental data with the background subtracted and the high temperature resistance normalized to that of the normal state resistance,  $R_N$ . The blue curve represents the theoretical fit using LAMH (Eq. (2)). The parameter values obtained are  $T_c=60$  K,  $A=0.09$ . The red line indicates the theoretical fit using LAMH plus MQT (Eq. (4)). The parameter values obtained by the fit are  $A_1=0.10$ ,  $A_2=0.13$ ,  $B=0.89$ . The addition of the MQT component is seen to be important to the fit below 10 K.

In addition, the magnetic field has little effect on the 1D superconducting system unless the magnetic field is extremely high. This is due to the fact that the 4 Å carbon nanotube arrays, if they have cross sections that are a few nanometers, will have very small magnetic susceptibility (which varies quadratically with the array diameter). For the normal state of 4 Å SWNTs the resistance didn't change under various magnetic fields, which indicates the magnetic susceptibility of 4 Å SWNTs is quite small. A detailed description of the LAMH theory is given in the [supplementary material](#), where we show that the theory explains not only the smooth resistance decrease as shown in Fig. 6, but also the appearance of nonlinear I-V behavior at small bias current as shown in Fig. 8. The latter is attributed to the dependence of the barrier height (reflected in the magnitude of the parameter  $A_1$ ) on the current density as shown in Fig. S2 (where the current current density is directly proportional to the winding number  $n$ ) of the [supplementary material](#).

The bias current dependence of differential resistance at different temperatures is shown in Fig. 8. We note that there is a well-defined resistance dip when temperature was maintained at 2 K. This resistance dip rules out the possibility of charge density waves and Tomonaga-Luttinger behaviors, both prominent possibilities for 1D conductors. This is because for charge density waves and Tomonaga-Luttinger liquid, the current dependence of the differential resistance should present a peak. In contrast, here the differential resistance increased smoothly as the bias current was increased. The behavior was consistent with 1D superconductivity (see [supplementary material](#)). The critical current of this sample was about 20  $\mu$ A. Moreover, the differential resistance dip became more

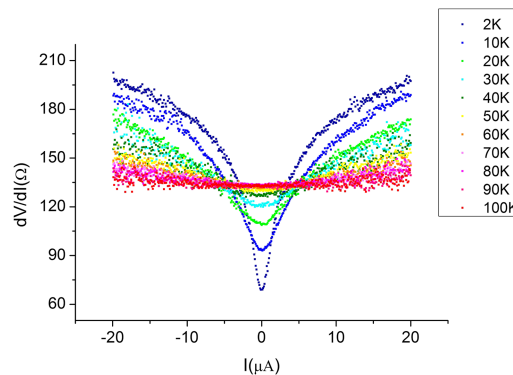


FIG. 8. The differential resistance vs. the bias current under different temperatures. The differential resistance dip is well developed at 2 K, and vanished when the temperature was raised above 60 K.

shallow as temperature was raised. The resistance dip disappeared completely after the temperature exceeded 90 K, beyond which the 1D superconductivity fades away.

There have been numerous theoretical studies on carbon nanotube superconductivity, based on the experimental observations. Pure graphite is not known to be superconducting, as the honeycomb lattice structure of graphene dictates weak electron-phonon coupling owing to its symmetry. However, when graphene is rolled into metallic carbon nanotubes with very small diameters, the original lattice symmetry of graphene is broken and electron-phonon coupling can emerge.<sup>22</sup> However, electron-phonon coupling in conducting 1D materials can have two divergent consequences—Peierls distortion that leads to an insulating (or semiconducting) state, or the 1D superconductivity. If Peierls distortion occurs at a higher transition temperature than the 1D superconductivity, then the latter will be suppressed, and vice versa. To investigate which option is theoretically preferred for the 4 Å SWNTs, second order renormalization group calculations were carried out.<sup>24</sup> For an array of aligned (5,0) carbon nanotubes separated center-to-center by 13.6 Angstroms, the dielectric screening effect can significantly reduce the electron-electron interaction, thereby making superconducting state the preferred ground state of the system. Hence in our template-grown 4 Å SWNTs, we expect the superconducting condensate to appear in small arrays, or bundles, of aligned nanotubes. The lateral dimension of these small arrays is expected to be a few nanometers.

#### IV. CONCLUSION

By making use of high quality micro platelet AFI crystals as the template, in conjunction with the approach of using two carbon sources in successive CVD processes, we have successfully fabricated 4 Å SWNTs embedded AFI with a very high pore filling factor (91%). For this new CVD method of growing 4 Å SWNTs, 1D fluctuating superconductivity was observed. The resistance decreased smoothly as a function of temperature, and the differential resistance measurement revealed a dip that disappeared above the 1D superconductivity initiation temperature, consistent with the temperature variation of resistance. The high 1D superconductivity initiation temperature, around 60 K, can be attributed to the high filling factor of the pores by the metallic (3,3) and (5,0) carbon nanotubes. This can greatly increase the effective dielectric constant of the sample, which can have a significant effect in the dielectric screening of the repulsive electron-electron interaction in the nanotubes, effectively enhancing the temperature at which the 1D superconducting condensate appears.<sup>24</sup>

#### SUPPLEMENTARY MATERIAL

See [supplementary material](#) for the LAMH theory.

#### ACKNOWLEDGMENTS

This work has been supported by the Research Grants Council of Hong Kong, Grants HKUST9/CRF/08 and RGC 16304314.

#### APPENDIX A: SYNTHESIS OF MICRO PLATELET AFI CRYSTALS

The micro platelet AFI crystals were synthesized by the hydrothermal method. The ingredients used in the synthesis were aluminum oxide, phosphorus pentoxide, silicon dioxide and triethanolamine (TEA). The molar composition of the solution was 1 Al<sub>2</sub>O<sub>3</sub>: 0.8 P<sub>2</sub>O<sub>5</sub>: 1 SiO<sub>2</sub>: 3.5 TEA: 50 H<sub>2</sub>O. The synthesis process is as follows. First 5.68 g of H<sub>3</sub>PO<sub>4</sub> (85%, Panreac) was mixed with 22.8 ml deionized (DI) water. Then the mixture was placed in an ice-water bath, and 4.42 g of pseudoboehmite (Catapal A, SASOL) was added to the solution and stirred for 1 hour. Next 4.62 g of silica solution (40 wt%, Ludox HS-40, Sigma-Aldrich) was added and stirred for another 1 hour. The resulting solution was taken out from the ice-water bath and stirred for 12 hours at room temperature to form a uniform precursor gel. The gel was transferred to a 100 ml Teflon autoclave and placed in a microwave oven (MARS-5, CEM, maximum power 1600 W), and the reaction mixture was rapidly heated to 180 °C within 1.5 min (microwave power, 1600 W) and maintained at that

temperature for a duration of 2.5 hours (microwave power, 400 W). When synthesis was finished the autoclave was cooled to room temperature, and the resulting solid product AFI was washed, collected by centrifugation and dried at 120 °C.

## APPENDIX B: CVD PROCESSES

The micro platelet AFI crystals were heated in oxygen atmosphere at 800 °C for 6 hours in order to burn off the precursor TEA molecules inside the linear channels. Then the carbon source was introduced as feedstock to grow the carbon nanotubes. We tried three different methods to produce carbon nanotubes as illustrated in Fig. 9 below. For method (a), C<sub>2</sub>H<sub>4</sub> was used as the carbon source. Empty AFI crystals were heated at 480 °C in C<sub>2</sub>H<sub>4</sub> with a pressure of 6 atmospheres for 10 hours. For method (b), CH<sub>4</sub> was used as the carbon source. Empty AFI crystals were heated at 800 °C in 6 atmospheres of CH<sub>4</sub> for 10 hours. For method (c), both C<sub>2</sub>H<sub>4</sub> and CH<sub>4</sub> were used as carbon sources in two successive rounds. First the empty AFI crystals were heated at 480 °C in 6 atmosphere of C<sub>2</sub>H<sub>4</sub> for 10 hours. Subsequently they were heated in 6 atmospheres of CH<sub>4</sub> for another 10 hours. All three methods can growth 4 Å SWNTs embedded in AFI (noted as SWNTs@AFI). However, samples fabricated by the three methods have different carbon contents and filling factors. They were characterized by both Raman spectra and thermal gravimetric analysis (TGA), as detailed in the main text.

It should be noted that by heating ethylene at 480 °C and methane at 800 °C, we avoided the formation of amorphous carbon on the surface of the crystals, which can be seen from the scanning electron microscope image. That is in contrast to the previous experience when we heated ethylene at temperatures of over 700 °C, which had created an excessive amount of amorphous carbon on the surface of the crystals.

## APPENDIX C: DEVICE FABRICATION FOR TRANSPORT MEASUREMENTS

The fabrication process is as follows. A thin layer of photoresist (950 PMMA 9 A) was coated on the surface of the glass film substrate. Then crystals of SWNTs@AFI were dispersed on the photoresist and heated on hotplate at 180 °C for 90 seconds. This process fixed the crystals on the surface of glass substrate and facilitated the subsequent process. A layer of adhesive Ti with a thickness of 5 nm was coated on the crystal by sputtering, followed by a layer of Au with a thickness of 60 nm. Focused

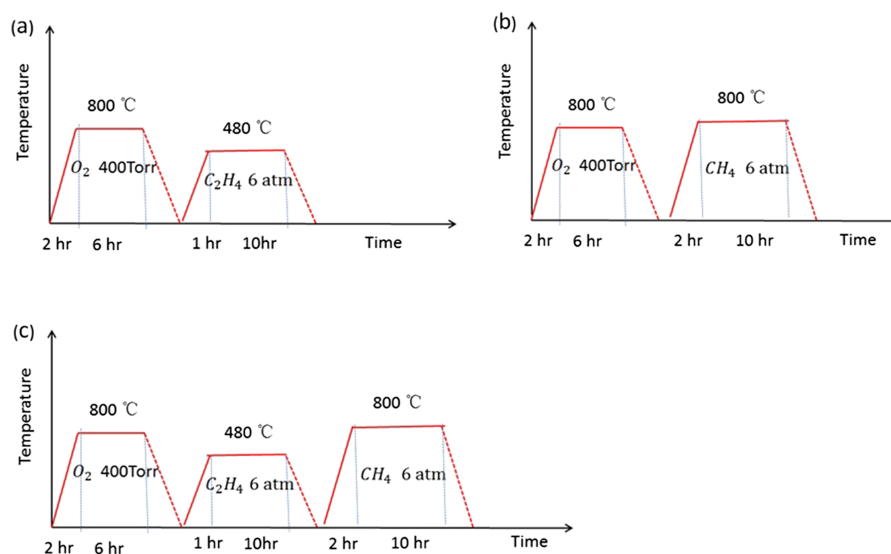


FIG. 9. Schematics of the three methods of fabricating 4 Å SWNTs. (a) Using 6 atmospheres of ethylene as the carbon source. (b) Using 6 atmospheres of methane as the carbon source. (c) Using 6 atmospheres of ethylene and then 6 atmospheres of methane as the carbon sources in successive rounds of heating.

ion beam (FIB) was used to select one crystal that stands on its sidewall, and the Ti/Au film on its surface was etched in a designed pattern (as shown in Fig. 6(a)) to get the four-lead electrical contact geometry. The separation between the electrodes is around 100 nm.

- <sup>1</sup> A. Oberlin, M. Endo, and T. Koyama, "Filamentous growth of carbon through benzene decomposition," *J. Cryst. Growth* **32**, 335–349 (1976).
- <sup>2</sup> S. Iijima, "Helical microtubules of graphitic carbon," *Nature* **354**, 56–58 (1991).
- <sup>3</sup> A. Javey, J. Guo, Q. Wang, M. Lundstrom, and H. Dai, "Ballistic carbon nanotube field-effect transistors," *Nature* **424**, 654–657 (2003).
- <sup>4</sup> S. J. Tans, A. R. M. Verschueren, and C. Dekker, "Room-temperature transistor based on a single carbon nanotube," *Nature* **393**, 49–52 (1998).
- <sup>5</sup> P. W. Barone, S. Baik, D. A. Heller, and M. S. Strano, "Near-infrared optical sensors based on single-walled carbon nanotubes," *Nature Materials* **4**, 86–92 (2005).
- <sup>6</sup> F. Wang, G. Dukovic, L. E. Brus, and T. F. Heinz, "The optical resonances in carbon nanotubes arise from excitons," *Science* **308**, 838–841 (2005).
- <sup>7</sup> J. N. Coleman, U. Khan, W. J. Blau, and Y. K. Gun'ko, "Small but strong: A review of the mechanical properties of carbon nanotube–polymer composites," *Carbon* **44**, 1624–1652 (2006).
- <sup>8</sup> M.-F. Yu, B. S. Files, S. Arepalli, and R. S. Ruoff, "Tensile loading of ropes of single wall carbon nanotubes and their mechanical properties," *Phys. Rev. Lett.* **84**, 5552–5555 (2000).
- <sup>9</sup> V. K. Upadhyayula, S. Deng, M. C. Mitchell, and G. B. Smith, "Application of carbon nanotube technology for removal of contaminants in drinking water: A review," *Sci. Total Environ.* **408**, 1–13 (2009).
- <sup>10</sup> D. Zhang, K. Ryu, X. Liu, E. Polikarpov, J. Ly, M. E. Tompson, and C. Zhou, "Transparent, conductive, and flexible carbon nanotube films and their application in organic light-emitting diodes," *Nano Lett.* **6**, 1880–1886 (2006).
- <sup>11</sup> R. H. Baughman, C. Cui, A. A. Zakhidov, Z. Iqbal, J. N. Barisci, G. M. Spinks, G. G. Wallace, A. Mazzoldi, D. De Rossi, A. G. Rinzler, O. Jaszchinski, S. Roth, and M. Kertesz, "Carbon nanotube actuators," *Science* **284**, 1340–1344 (1999).
- <sup>12</sup> W. A. de Heer, A. Châtelain, and D. Ugarte, "A carbon nanotube field-emission electron source," *Science* **270**, 1179–1180 (1995).
- <sup>13</sup> D. H. Robertson, D. W. Brenner, and J. W. Mintmire, "Energetics of nanoscale graphitic tubules," *Phys. Rev. B* **45**, 12592–12595 (1992).
- <sup>14</sup> S.-i. Sawada and N. Hamada, "Energetics of carbon nano-tubes," *Solid State Commun.* **83**, 917–919 (1992).
- <sup>15</sup> L.-C. Qin, X. Zhao, K. Hirahara, Y. Miyamoto, Y. Ando, and S. Iijima, "The smallest carbon nanotube," *Nature* **408**, 50–50 (2000).
- <sup>16</sup> N. Wang, Z. K. Tang, G. D. Li, and J. S. Chen, "Single-walled 4 Å carbon nanotube arrays," *Nature* **408**, 50–51 (2000).
- <sup>17</sup> I. L. Li, G. D. Li, H. J. Liu, C. T. Chan, and Z. K. Tang, "Chirality-dependent curvature effect in smallest single-walled carbon nanotubes," *Appl. Phys. Lett.* **82**, 1467–1469 (2003).
- <sup>18</sup> Z. M. Li, Z. K. Tang, H. J. Liu, N. Wang, C. T. Chan, R. Saito, S. Okada, G. D. Li, J. S. Chen, N. Nagasawa, and S. Tsuda, "Polarized absorption spectra of single-walled 4 Å carbon nanotubes aligned in channels of an AlPO<sub>4</sub>-5 single crystal," *Phys. Rev. Lett.* **87**, 127401 (2001).
- <sup>19</sup> H. J. Liu and C. T. Chan, "Properties of 4 Å carbon nanotubes from first-principles calculations," *Phys. Rev. B* **66**, 115416 (2002).
- <sup>20</sup> Z. K. Tang, L. Zhang, N. Wang, X. X. Zhang, G. H. Wen, G. D. Li, J. N. Wang, C. T. Chan, and P. Sheng, "Superconductivity in 4 Å single-walled carbon nanotubes," *Science* **292**, 2462–2465 (2001).
- <sup>21</sup> Z. K. Tang, Z. M. Li, I. L. Li, X. Zhang, N. Wang, J. Wang, and P. Sheng, "Electrical and optical properties of ultra-small carbon nanotubes arrayed in channels of zeolite single crystals," *Mater. Trans.* **44**, 2066–2069 (2003).
- <sup>22</sup> L. X. Benedict, V. H. Crespi, S. G. Louie, and M. L. Cohen, "Static conductivity and superconductivity of carbon nanotubes: Relations between tubes and sheets," *Phys. Rev. B* **52**, 14935–14940 (1995).
- <sup>23</sup> R. Barnett, E. Demler, and E. Kaxiras, "Electron-phonon interaction in ultrasmall-radius carbon nanotubes," *Phys. Rev. B* **71**, 035429 (2005).
- <sup>24</sup> T. Zhang, M. Y. Sun, Z. Wang, W. Shi, and P. Sheng, "Crossover from Peierls distortion to one-dimensional superconductivity in arrays of (5,0) carbon nanotubes," *Phys. Rev. B* **84**, 245449 (2011).
- <sup>25</sup> J. González and E. Perfetto, "Coulomb screening and electronic instabilities of small-diameter (5,0) nanotubes," *Phys. Rev. B* **72**, 205406 (2005).
- <sup>26</sup> K. Kamide, T. Kimura, M. Nishida, and S. Kurihara, "Singlet superconductivity phase in carbon nanotubes," *Phys. Rev. B* **68**, 024506 (2003).
- <sup>27</sup> J. S. Langer and V. Ambegaokar, "Intrinsic resistive transition in narrow superconducting channels," *Phys. Rev.* **164**, 498–510 (1967).
- <sup>28</sup> D. E. McCumber and B. I. Halperin, "Time scale of intrinsic resistive fluctuations in thin superconducting wires," *Phys. Rev. B* **1**, 1054–1070 (1970).
- <sup>29</sup> N. Giordano, "Evidence for macroscopic quantum tunneling in one-dimensional superconductors," *Phys. Rev. Lett.* **61**, 2137 (1988).
- <sup>30</sup> D. S. Golubev and A. D. Zaikin, "Quantum tunneling of the order parameter in superconducting nanowires," *Phys. Rev. B* **64**, 014504 (2001).
- <sup>31</sup> C. N. Lau, N. Markovic, M. Bockrath, A. Bezryadin, and M. Tinkham, "Quantum phase slips in superconducting nanowires," *Phys. Rev. Lett.* **87**, 217003 (2001).
- <sup>32</sup> Q. Chen, Z. Wang, Y. Zheng, W. Shi, D. Wang, Y.-C. Luo, B. Zhang, J. Lu, H. Zhang, J. Pan, C.-Y. Mou, Z. K. Tang, and P. Sheng, "New developments in the growth of 4 Å carbon nanotubes in linear channels of zeolite template," *Carbon* **76**, 401–409 (2014).

- <sup>33</sup> M. S. Dresselhaus, G. Dresselhaus, R. Saito, and A. Jorio, "Raman spectroscopy of carbon nanotubes," *Phys. Rep.* **409**, 47–99 (2005).
- <sup>34</sup> A. Jorio, A. G. Souza Filho, G. Dresselhaus, M. S. Dresselhaus, A. K. Swan, M. S. Ünlü, B. B. Goldberg, M. A. Pimenta, J. H. Hafner, C. M. Lieber, and R. Saito, "G-band resonant Raman study of 62 isolated single-wall carbon nanotubes," *Phys. Rev. B* **65**, 155412 (2002).
- <sup>35</sup> C. Fantini, A. Jorio, M. Souza, L. O. Ladeira, A. G. Souza Filho, R. Saito, G. G. Samsonidze, G. Dresselhaus, M. S. Dresselhaus, and M. A. Pimenta, "One-dimensional character of combination modes in the resonance Raman Scattering of carbon nanotubes," *Phys. Rev. Lett.* **93**, 087401 (2004).
- <sup>36</sup> J. Haruyama, A. Tokita, N. Kobayashi, M. Nomura, S. Miyadai, K. Takazawa, A. Takeda, and Y. Kanda, "End-bonding multiwalled carbon nanotubes in alumina templates: Superconducting proximity effect," *Appl. Phys. Lett.* **84**, 4714–4716 (2004).
- <sup>37</sup> I. Takesue, J. Haruyama, N. Kobayashi, S. Chiashi, S. Maruyama, T. Sugai, and H. Shinohara, "Superconductivity in entirely end-bonded multiwalled carbon nanotubes," *Phys. Rev. Lett.* **96**, 057001 (2006).
- <sup>38</sup> W. Shi, Z. Wang, Q. Zhang, Y. Zheng, C. Jeong, M. He, R. Lortz, Y. Cai, N. Wang, T. Zhang, H. Zhang, Z. Tang, P. Sheng, H. Muramatsu, Y. A. Kim, M. Endo, P. T. Araujo, and M. S. Dresselhaus, "Superconductivity in bundles of double-wall carbon nanotubes," *Sci. Rep.* **2**, 625 (2012).
- <sup>39</sup> M. Ferrier, A. Kasumov, R. Deblock, S. Guéron, and H. Bouchiat, "Induced and intrinsic superconductivity in carbon nanotubes," *J. Phys. D: Appl. Phys.* **43**, 374003 (2010).

## **Supplementary Materials**

**for**

**Observation of high  $T_c$  one dimensional superconductivity in**

**4 Angstrom carbon nanotube arrays**

*Bing Zhang, Yang Liu, Qihong Chen, Zhiping Lai, Ping Sheng*

### **One dimensional fluctuation superconductivity**

#### **Introduction and relevance to the experimental data**

The definition of a one dimensional (1D) superconductor is that the superconducting coherence length is larger than the cross sectional dimension of the 1D wire. When that happens, the superconducting wavefunction can be regarded as a constant at any given cross section, but can vary along the length direction  $x$  of the wire. Moreover, since any variation in the magnitude of the superconducting wavefunction, which represents the superconducting condensate density, requires a much larger energy than the phase of the wavefunction, hence it is usually the case that in the theory of 1D superconductors only the phase variation is considered as a function of  $x$ . In a long 1D superconductor (long meaning compared to the coherence length), the end effect of the wire can be neglected, hence its physics may be described by a ring, in which periodic boundary condition on the phase can be imposed. When that happens, only a phase change of  $2\pi$  is possible. But such a phase change would require the magnitude of the wavefunction vanish at least at one point along the length direction, which requires energy. Hence there is an energy barrier between  $2\pi$  phase change which is proportional to the cross sectional area of the wire. When the cross section is thin, the energy barrier is low, and thermal fluctuations can cause the phase changes in a regular manner, statistically speaking. Such fluctuation-initiated phase changes are called the “phase slip” mechanism. When that happens, the Josephson relation (see below) dictates a voltage would appear, which is equivalent to say that resistance

appears. The above is a qualitative description of the phase slip mechanism and its relation to the appearance of resistance in 1D superconductors. Below we give a more detailed mathematical description of the theory behind it, and the behavior of the predicted resistance that appears as a result of the phase slip mechanism. In short, what the theory predicts are (1) the resistance should vary smoothly as a function of temperature, and (2) there should be a nonlinear current-voltage (I-V) behavior at small bias currents. Both of these predicted behaviors are seen in our experiments, consistent with the theory of 1D superconductors.

### The Ginzburg-Landau equation

The properties of the 1D superconductors can be described by the Langer–Ambegaokar–McCumber–Halperin (LAMH) theory<sup>1,2</sup>, which is based on the Ginzburg-Landau (GL) equation. For the 1D superconductivity, dissipation occurs when thermal fluctuation causes the order parameter wavefunction to vanish at some point along the wire, and the phase of the wavefunction to change by  $2\pi$ . As a consequence, the 1D superconductor can have finite resistance at finite temperature below the transition temperature. In general, the diameter of the 1D superconductor is much smaller than the coherence length. Thus the parameters of GL can be regarded as a constant over the cross-sectional area and are a function of  $x$  only, where  $x$  denotes the axial coordinate. The Ginzburg-Landau free-energy functional has the form<sup>3</sup>:

$$F[\psi(x)] = \sigma \int dx \left[ \frac{\hbar^2}{2m^*} |\nabla \psi(x)|^2 + \alpha |\psi(x)|^2 + \frac{\beta}{2} |\psi(x)|^4 \right], \quad (\text{S1})$$

where  $\sigma$  is the cross-sectional area of the 1D superconductor,  $\alpha$  and  $\beta$  are the phenomenological parameters. The time evolution of  $\psi$  is governed by the time-dependent Ginzburg-Landau equation:

$$\gamma \frac{\partial}{\partial t} \psi = -\frac{1}{\sigma} \frac{\delta F[\psi]}{\delta \psi} + \zeta = \frac{\hbar^2}{m^*} \nabla^2 \psi - 2\alpha \psi - 2\beta |\psi|^2 \psi + \zeta, \quad (\text{S2})$$

where  $\gamma$  is a viscosity coefficient and  $\zeta$  is the Langevin white noise, intended to model thermal fluctuations. The noise leads to a random variation of  $\psi$ . It is convenient to use the dimensionless form in computation:

$$F[\bar{\psi}(\bar{x})] = \int d\bar{x} \left[ \frac{1}{2} |\bar{\nabla} \bar{\psi}(\bar{x})|^2 - \frac{1}{2} |\bar{\psi}(\bar{x})|^2 + \frac{1}{4} |\bar{\psi}(\bar{x})|^4 \right]. \quad (\text{S3})$$

The over-bar denotes the dimensionless quantities, obtained with  $F$  scaled by  $\sigma\xi\alpha_0^2(T_c - T) / \beta = \varepsilon_0$ , which is the superconducting condensation energy for a volume  $\sigma\xi$ ,  $\psi$  is scaled by  $\sqrt{-\alpha / \beta}$  and  $x$  is scaled by the correlation length  $\xi(T)$ . The dimensionless form of the GL equation is obtained from Eq. (S3) through functional variation:

$$\frac{\partial}{\partial \bar{t}} \bar{\psi} = -\frac{\delta \bar{F}[\bar{\psi}]}{\delta \bar{\psi}} + \bar{\zeta} = \bar{\nabla}^2 \bar{\psi} + \bar{\psi} - |\bar{\psi}|^2 \bar{\psi} + \bar{\zeta}, \quad (\text{S4})$$

where time is scaled by  $\tau(T) = -\gamma / \alpha$ .

### Solution for the metastable superconducting current states

For a closed superconducting ring we can use the periodic boundary condition  $\psi(-l/2) = \psi(l/2)$ , where  $l$  is the circumference of a ring. Then we can get the metastable current carrying states  $\psi_n$  from the stationary Ginzburg–Landau equation

$$0 = \frac{\partial}{\partial \bar{t}} \bar{\psi} = \bar{\nabla}^2 \bar{\psi} + \bar{\psi} - \beta |\bar{\psi}|^2 \bar{\psi}, \quad (\text{S5a})$$

which yields the solution

$$\bar{\psi}_n = \sqrt{1 - k_n^2} e^{ik_n x}, k_n = 2\pi n / l, \quad (\text{S5b})$$

where  $k_n$  is the wave vector and  $n$  is an integer, called the winding number.

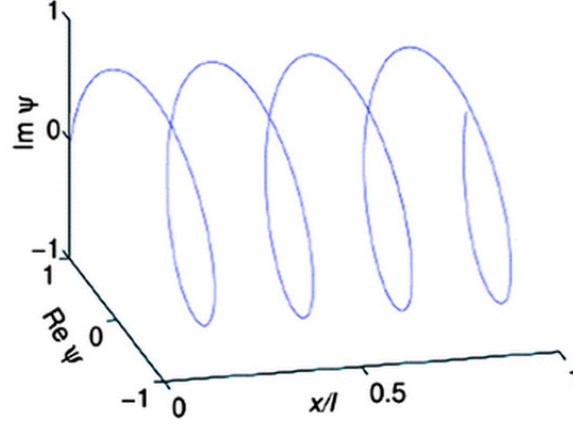


**Figure S1.** The order parameter  $\psi$  for a 1D superconductor with a winding number of four<sup>4</sup>. Since the magnitude of the wavefunction is regarded as rigid, a helical configuration naturally emerges to depict the phase change along  $x$ .

Owing to the fact that the variation of wave function magnitude involves much larger energy than the phase variation, the magnitude of wave function is rather rigid at a fixed temperature below  $T_c$ . In order to depict such a state a picture of this meta-state is shown in figure S1, which involves only the phase variation as a function of  $x$ . In quantum mechanics, the current density in the  $\bar{\psi}_n$  state is given by the spatial derivative of the wavefunction:

$$J_n = \bar{\psi}^* \frac{\partial}{\partial x} \bar{\psi} = (1 - k_n^2) k_n, \quad (\text{S6})$$

where  $|k_n| < k_c$ , with  $k_c = 1/\sqrt{3}$  being the critical upper bound for  $k_n$ . Larger winding number  $n$  corresponds to larger carrying current as well as a higher free energy of the metastable state. As illustrated in figure S2, the scaled free energy  $F$  is plotted as a function of the arc length  $s$  in the  $\psi(x)$  functional space. It is evaluated along the minimal energy path connecting a sequence of the meta-stable  $(-8, -7, \dots, -1, 1, \dots, 7, 8)$  and stable states ( $n = 0$ ). This figure was numerically evaluated by using the string method<sup>4</sup>.

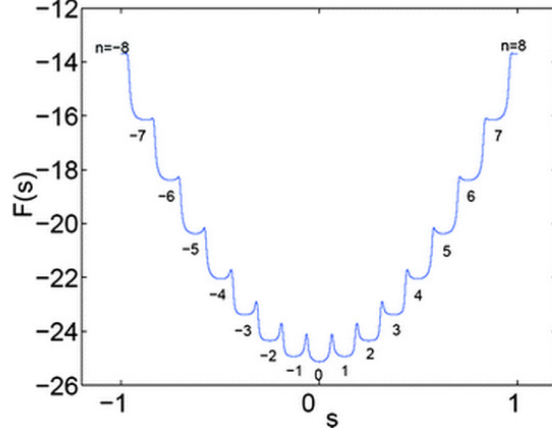


**Figure S2.** Free energy  $F$  evaluated along the minimal energy path connecting a sequence of the meta-stable ( $-8, -7, \dots, -1, 1, \dots, 7, 8$ ) and the stable state ( $n = 0$ ). Here  $s$  represents the arc length along the minimal energy path in the functional space of  $\psi(x)$ . Each metastable minimum represents a winding number configuration<sup>4</sup>. It should be noted that the barrier height separating the different metastable states, each characterized by  $n$ , decreases with increasing current level (increasing  $n$ ).

We can see that there is a potential barrier between neighboring metastable states. Moreover, this potential barrier becomes larger for the lower current-carrying states. This will have implications for the nonlinear I-V characteristic as a function of the bias current, described below. The carrying current does not generate any voltage if the wave function remains in a metastable state, which means that the system is still superconducting. Nevertheless, in the presence of thermal fluctuations, one metastable state can cross the potential barrier and transit to another metastable state (more probably the lower free energy one). Therefore, these metastable states just have a finite lifetime in a thermal bath. Let us consider a 1D superconductor which is connected to a constant (bias) current source. If a metastable state  $n$  transits to the lower free energy metastable state  $n-1$ , then the carrying current of the 1D superconductor will decrease. However, the constant (bias) current source will push the system back to the metastable state  $n$  again in order to maintain the current at a fixed value. Hence dissipation would occur in this process, which is equal to the work done by the external (constant current) source. Another way to explain the same thing is that the thermally induced transitions between the metastable states will generate a

voltage. The magnitude of the voltage is described by the following Josephson relation:

$$2\pi\Gamma_{ps} = 2eV / \hbar, \quad (\text{S7a})$$

with

$$\Gamma_{ps} = \Omega \exp(-\Delta F / k_B T), \quad (\text{S7b})$$

where  $\Gamma_{ps}$  is the phase slip rate,  $\Omega$  is the transition rate pre-factor, and  $\Delta F$  is the energy barrier. There is a temperature dependence of the energy barrier, given by

$$\Delta F = (8\sqrt{2}/3)(H_C^2 / 8\pi)\sigma\xi,$$

where  $H_C$  and  $\xi$  are the thermodynamic critical field and the coherence length,

$H_C = H_{C0}[1 - (T/T_C)^2]$  and  $\xi = \xi_0 / (1 - T/T_C)^{1/2}$ . we can see that the energy barrier

is proportional to the cross section area  $\sigma$  of the superconductor.

After simplification we get

$$\frac{\Delta F}{k_B T} = \frac{\sqrt{2}H_{C0}^2\sigma\xi_0}{3\pi k_B T_C} \frac{T_C}{T} \frac{[1 - (T/T_C)^2]^2}{(1 - T/T_C)^{1/2}} = A \frac{T_C}{T} \left(1 + \frac{T}{T_C}\right)^2 \left(1 - \frac{T}{T_C}\right)^{3/2}, \quad (\text{S8})$$

where  $A = \frac{\sqrt{2}H_{C0}^2\sigma\xi_0}{3\pi k_B T_C}$  is a dimensionless constant. By definition the resistance is the

ratio of voltage divided by the bias current that is supplied by the current source.

Hence

$$R = V / I = \hbar\pi\Gamma_{ps} / eI = R_N \exp(-\Delta F / k_B T) = R_N \exp\left[-A \frac{T_C}{T} \left(1 + \frac{T}{T_C}\right)^2 \left(1 - \frac{T}{T_C}\right)^{3/2}\right],$$

or

$$R = R_N \exp\left[-A \frac{T_C}{T} \left(1 + \frac{T}{T_C}\right)^2 \left(1 - \frac{T}{T_C}\right)^{3/2}\right]. \quad (\text{S9})$$

where  $R_N$  denotes the normal state resistance. With decreasing temperature the resistance decreases smoothly if the parameter  $A$  is small, i.e., small cross sectional

area. For a fixed temperature, the resistance would be larger for higher bias current-carrying states as a consequence of the increased transition rate.

### **Smooth temperature variation of resistance and the $dV/dI$ dip**

The basic concept of LAMH theory gives us a simple picture about how a 1D superconductor acquires finite resistance. From Eq. (S9), it is easily seen that the resistance must decrease as temperature decreases, in a continuous and smooth manner. Moreover, since the barrier  $\Delta F$  is large for small bias current and smaller for large bias current as noted above, it follows that the I-V characteristic should be nonlinear (since  $\Delta F$  appears in the exponent), i.e., the resistance should be small at small bias current and increases with increasing bias current. That is precisely the differential resistance dip observed in our experiment.

It is noteworthy that the height of the potential barriers separating the meta-stable states is directly proportional to the cross-sectional area of 1D superconductor. Therefore, the transition rate exponentially decreases with an increasing cross-sectional area and the resistance vanishes as the system approaches 3D.

### **References**

- (1) Langer, J. S. & Ambegaokar, V. Intrinsic resistive transition in narrow superconducting channels. *Phys. Rev.* **164**, 498-510 (1967).
- (2) McCumber, D. E. & Halperin, B. I. Time scale of intrinsic resistive fluctuations in thin superconducting wires. *Phys. Rev. B* **1**, 1054-1070 (1970).
- (3) Wang, Z., Shi, W., Lortz, R. & Sheng, P. Superconductivity in 4-Angstrom carbon nanotubes—A short review. *Nanoscale* **4**, 21-41 (2012).
- (4) Qian, T., Ren, W. & Sheng, P. Current dissipation in thin superconducting wires: A numerical evaluation using the string method. *Phys. Rev. B* **72**, 014512 (2005).